Energy Storage Materials 63 (2023) 102962

Contents lists available at ScienceDirect

Energy Storage Materials

journal homepage: www.elsevier.com/locate/ensm

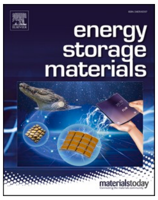

Overlithiation-driven structural regulation of lithium nickel manganese oxide for high-performance battery cathode

Yuchen Tan [a], Rui Wang [b], Xiaoxiao Liu [c], Junmou Du [a,d], Wenyu Wang [a], Renming Zhan [a], Shuibin Tu [a], Kai Cheng [a], Zihe Chen [a], Zhongyuan Huang [b], Yinguo Xiao [b], Yongming Sun [a,*]

[a] Wuhan National Laboratory for Optoelectronics, Huazhong University of Science and Technology, Wuhan 430074, China
[b] School of Advanced Materials, Peking University, Shenzhen Graduate School, Shenzhen 518055, China
[c] Xiamen Hithium Energy Storage Technology Co., Ltd., Xiamen 361100, China
[d] Deepal Automobile Technology Co., Ltd., Chongqing 401120, China

ARTICLE INFO

Keywords:
Spinel $LiNi_{0.5}Mn_{1.5}O_4$
Overlithiation
Structural stability
Donable capacity
Lithium-ion batteries

ABSTRACT

Spinel $LiNi_{0.5}Mn_{1.5}O_4$ (LNMO) is a promising cathode material due to its high operation voltage, cobalt free nature and low cost. High energy density of batteries could be realized by coupling LNMO with high-capacity Si based anodes, before which large active lithium loss at the anode should be addressed. Pre-insertion of additional lithium (Li, x) into LNMO, namely overlithiaition of LNMO (L_{1+x}NMO) here, becomes a promising approach for active Li compensation. Understanding the materials structure and property evolution of L_{1+x}NMO and their further effect on electrochemical behavior is crucial. Although spinel LNMO could endure a certain amount of extra Li, its excessive insertion could cause degradation in materials structure, interfacial stability and electrochemical performance due to the introduction of large strain, grain boundaries and immoderate reduction of Mn element. $L_{1.4}$NMO showed a tradeoff between donable lithium-ion capacity and electrochemical cycling stability among the investigated L_{1+x}NMO ($x = 0$, 0.2, 0.4, 0.6 and 1) samples. $L_{1.4}$NMO||Si/C cell presented a reversible capacity of 121.7 mAh g^{-1} and energy density of 429 Wh kg^{-1}, achieving over 50 % improvement than that of LNMO||Si/C cell.

1. Introduction

$LiNi_{0.5}Mn_{1.5}O_4$ (LNMO) with high working potential (~4.7 V *vs.* Li/Li^+), cobalt free nature and low cost is becoming an attractive cathode choice for high-performance lithium-ion batteries [1–5]. Coupling LNMO cathode with Si based anodes to replace the state-of-art graphite anode could increase the energy density of batteries due to its much higher theoretical specific capacity (e.g., 4200 mAh g^{-1} for Si *vs.* 372 mAh g^{-1} for graphite). However, low initial Coulombic efficiency (ICE) of current Si based anodes would irreversibly consume limited active lithium (Li) from LNMO with theoretical capacity of 146.7 mAh g^{-1} and reduce the energy density of batteries [6]. Till now, abundant researches have been conducted on Li compensation at both the anode and the cathode [7–9]. Direct implantation of active Li into Si-based anodes goes straight [6,10–16]. However, the as-formed Li_xSi shows high chemical reactivity and is usually moisture sensitive, associating with safety concerns in large-scale manufacture. This makes it challenging to implant anode prelithiation approaches into practical application at the current stage. In contrast, Li compensation at the cathode side, including electrochemical prelithiation and chemical prelithiation, is relatively stable and adaptive to the current battery fabrication conditions [17–22]. Compared to electrochemical prelithiation, chemical prelithiation does not need the assembly and disassembly of cells and could be conducted at both material and electrode levels, which shows more practical feasibility.

Spinel LNMO allows the insertion of extra active Li to form overlithiated LNMO (L_{1+x}NMO) [7,23–25]. Electrochemical and chemical approaches have been previously explored for the prelithiation of LNMO. For example, lithium pre-insertion into LNMO was conducted to achieve $L_{1.2}$NMO via electrochemical lithiation process and the full cell with such overlithiated cathode exhibited increased capacity [7]. A full overlithiation state of L_2NMO was realized through the reaction between LNMO and 1.6 M n-butyl-Li solution (hexanes as solvent) [23] and the reaction between LNMO and LiI in acetonitrile at 80°C with a six-fold excess of LiI [24], respectively. However, the correlation between structural stability and materials microstructure in the evolution

---

* Corresponding author.
E-mail address: yongmingsun@hust.edu.cn (Y. Sun).

https://doi.org/10.1016/j.ensm.2023.102962
Received 1 July 2023; Received in revised form 22 August 2023; Accepted 10 September 2023
Available online 11 September 2023

of LNMO overlithiation remains unexplored. Insights into the bulk structure and interfacial evolution of LNMO caused by overlithiation, and their effect on electrochemical cycling behavior could enhance scientific understanding of cathode overlithiation and provide guidance for materials design with rational structure and overlithiation degree for achieving the tradeoff between donable lithium-ion capacity and electrochemical cyclability.

In this work, we investigated an overlithiation degree (*x*)-mediated evolution of L_{1+x}NMO structure, including phases, lattice strain, grain boundaries and chemical/electrochemical reactivity, as well as their dependence on the electrochemical properties. With the increase of introduced Li, cubic LNMO gradually transformed to tetragonal L_2NMO phase. The phase transition initially started on the surface of particles and gradually spread into the interior of the active particle, accompanied by the generation of lattice strain, grain boundaries and changed interphase chemical/electrochemical properties. The overlithiation-degree tolerance of LNMO was analyzed based on the physicochemical properties and electrochemical stability. L_{1+x}NMO with deep overlithiation degree, such as $x = 1$ (L_2NMO), displayed serious structural degradation as well as high Mn^{3+} content, which caused fast collapse of the bulk structure and speeded up the parasitic reaction between active materials and electrolyte. $L_{1.4}$NMO delivered a reasonably high doable capacity of 52 mAh g^{-1} at the initial charge process and comparable electrochemical cyclability to LNMO at 0.5 *C* in regular carbonate electrolyte. $L_{1.4}$NMO||Si/C cell demonstrated 62.5 % increase in reversible capacity and 57.7 % increase in energy density in comparison to LNMO||Si/C cell (121.7 mAh g^{-1} and 429 Wh kg^{-1} for $L_{1.4}$NMO||Si/C, 74.9 mAh g^{-1} and 272 Wh kg^{-1} for LNMO||Si/C), due to the successful compensation for the initial lithium loss at the anode. Correlating structural evolution with electrochemical behavior caused by overlithiation provides valuable insights for rational cathode overlithiation design and can facilitate the development of high energy density lithium-ion batteries.

2. Results and discussion

To investigate the overlithiation degree (*x*)-mediated structural evolution of L_{1+x}NMO, samples with different overlithiation degrees (denoted as L_{1+x}NMO, $x = 0.2$, 0.4, 0.6 and 1) were fabricated via chemical prelithiation using reductive Li containing solution. As shown in Fig. 1a–c, with the increase of *x* in L_{1+x}NMO samples, the characteristic X-Ray Diffraction (XRD) peaks for LNMO phase (PDF 80-2162)

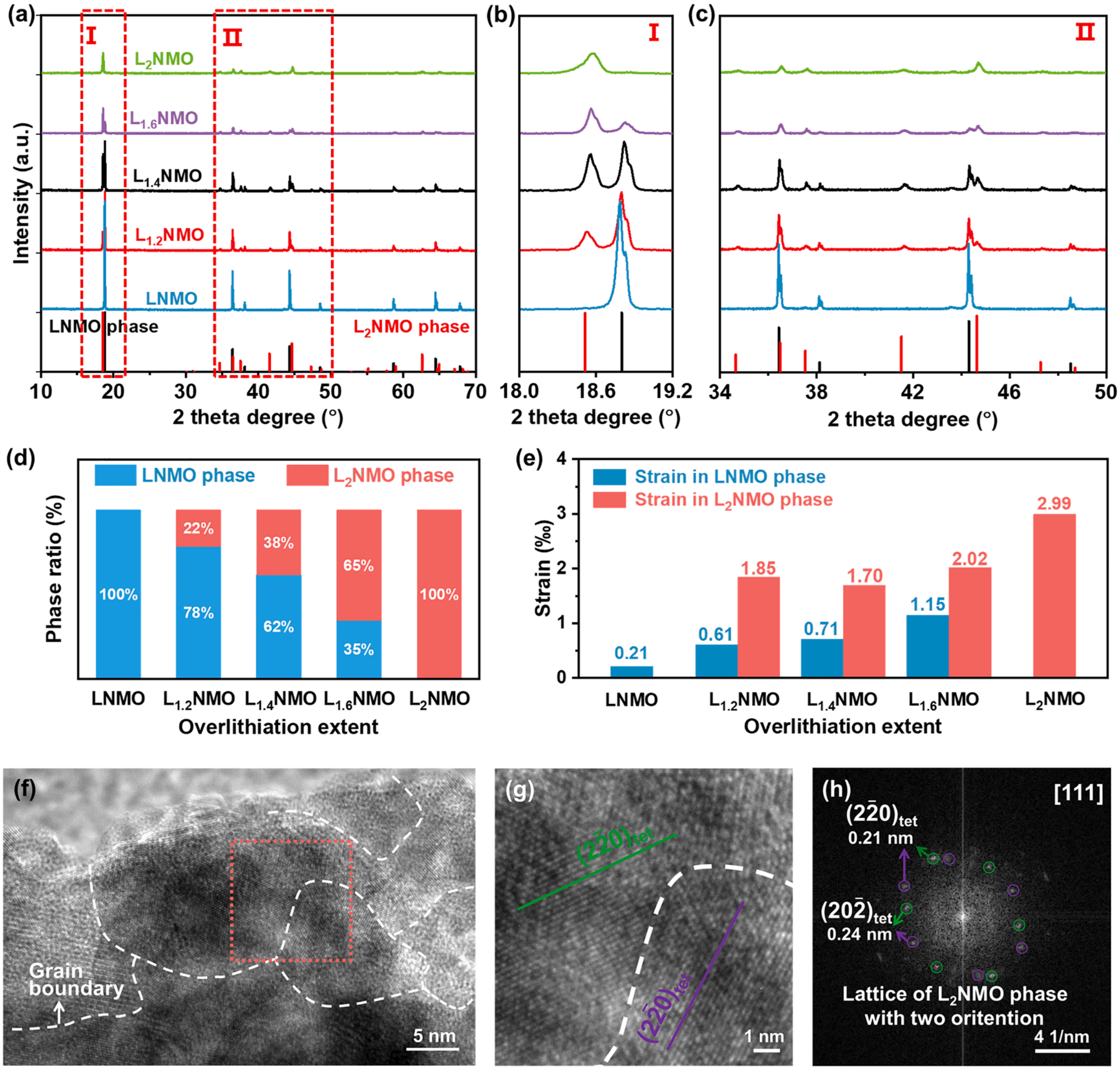

Fig. 1. (a-c) XRD patterns of L_{1+x}NMO samples ($x = 0$, 0.2, 0.4, 0.6 and 1). (d) The ratio of the two phases according to the XRD Rietveld refinement results. (e) The strain in LNMO phase and L_2NMO phase for a specific L_{1+x}NMO. (f) HRTEM image of L_2NMO sample. (g) HRTEM image and (h) the corresponding FFT image at a selected area.

gradually weakened, and that for L_2NMO phase appeared and gradually sharpened, indicating the gradual phase transition process accompanied by the continuous Li intercalation [23]. Detailed crystallographic information of L_{1+x}NMO samples with different prelithiation degrees were analyzed by rietveld refinement (Table S1 and Figs. S2, S3). When x reached 1 in L_{1+x}NMO, pristine cubic LNMO with *Fd-3m* space group was completely converted to pure tetragonal L_2NMO with $I4_1/amd$ space group. The intermediate L_{1+x}NMO samples with different overlithiation degrees exhibited different phase ratios of LNMO and L_2NMO (Fig. 1d). Typically, $L_{1.4}$NMO sample consisted of 62 % LNMO and 38 % L_2NMO phases. Moreover, the atomic concentrations of Li, Ni and Mn elements in all L_{1+x}NMO samples were also measured by inductively coupled plasma optical emission spectrometer (ICP-OES) (Table S2), which were overall in agreement with the results of rietveld refinement. Based on above results, accurate regulation of the practical Li amount in L_{1+x}NMO samples can be realized by this chemical overlithiation approach.

The average lattice strain in single-crystal was estimated by the Williamson−Hall method according to the XRD results (Fig. S2) [26,27]. For simplicity, we compared the strain in LNMO phase and L_2NMO phase, separately. Overall, the strain for single LNMO phase increased from 0.21 ‰ for pure LNMO sample, to 0.61 ‰ for $L_{1.2}$NMO sample, to 0.71 ‰ for $L_{1.4}$NMO sample, and 1.15 ‰ for $L_{1.6}$NMO sample. The increased tendency of strain dependence on x for L_2NMO phase in all the L_{1+x}NMO samples was also observed. The strain calculated based on L_2NMO phase increased to 1.85 ‰, 1.70 ‰, 2.02 ‰ and 2.99 ‰ for $L_{1.2}$NMO, $L_{1.4}$NMO, $L_{1.6}$NMO and L_2NMO samples, respectively. It was noted that at $x > 0.6$ or higher in L_{1+x}NMO sample, LNMO and L_2NMO phases both exhibited high values of strain (e.g., 1.15 ‰ and 2.02 ‰ for $L_{1.6}$NMO sample, respectively), suggesting that high overlithiation degree could cause structural instability. The structure of L_2NMO sample was further measured by high-resolution transmission electron micrograph (HRTEM) and abundant grain boundaries were observed (Fig. 1f). In the selected area (Fig. 1g), (2–20) planes of L_2NMO phase with different crystalline orientations were shown on two neighboring nanodomains (colored as green and purple, separately), which was again evidenced by the results of the corresponding fast Fourier transform (FFT) image (Fig. 1h) and inverse FFT image (Fig. S4). Random crystalline orientations of lattice were observed when enlarging the selected area (Fig. S5), indicating the formation of grain boundaries in the process of phase transformation. These results evidenced the lattice distortion and defect structure in highly overlithiated LNMO (such as L_2NMO), due to the large strain and excessive growth of grain boundaries.

The structure evaluation of L_{1+x}NMO sample during its chemical lithiation was further investigated by TEM and selected area electron

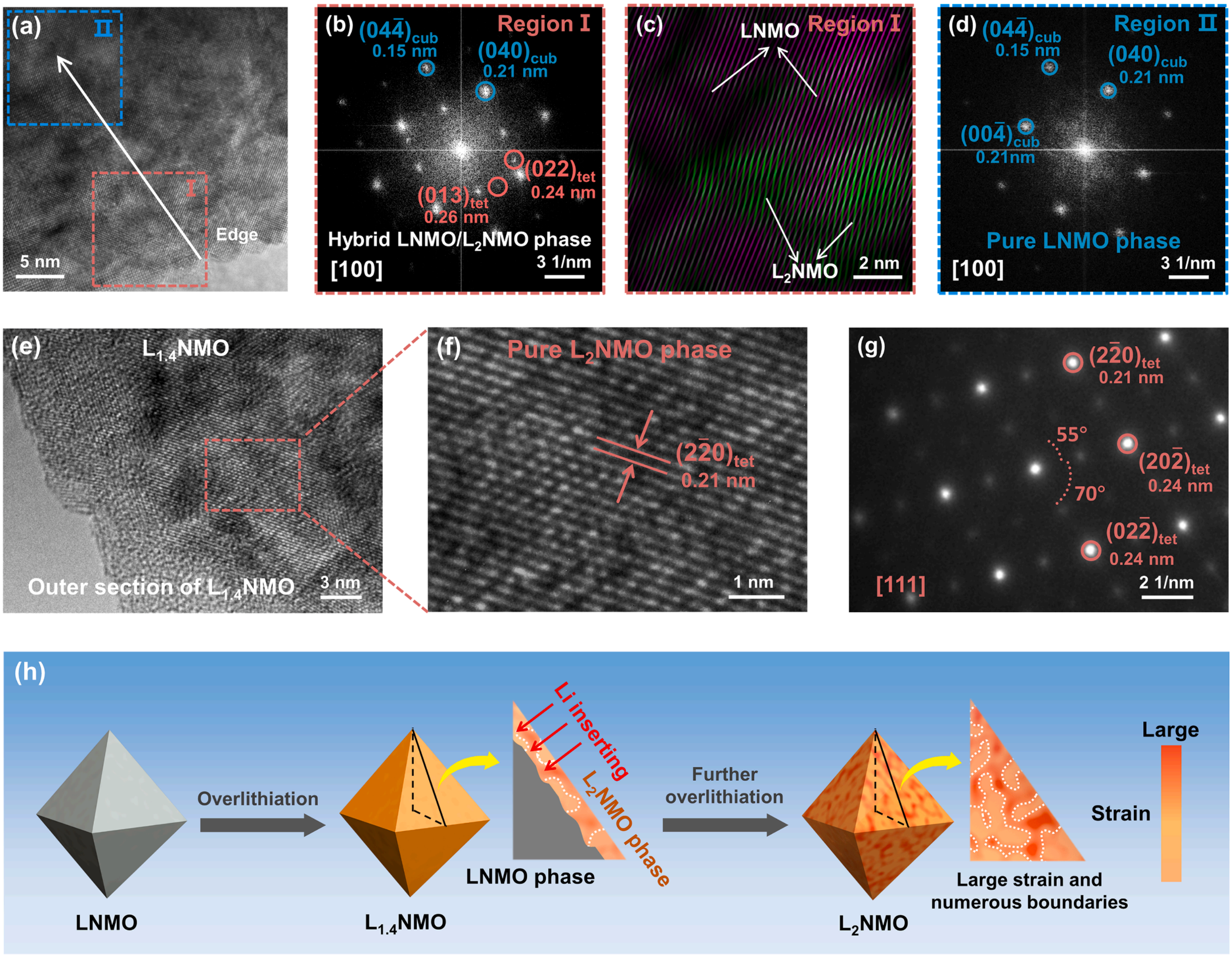

Fig. 2. (a) HRTEM image of $L_{1.05}$NMO sample. (b) FFT image at region I and (c) the corresponding inverse FFT image. (d) The FFT image at region II. (e, f) HRTEM images and (g) the corresponding SAED pattern of $L_{1.4}$NMO sample. (h) Schematic of structural evolution for LNMO during overlithiation.

diffraction (SAED). Fig. 2a showed a HRTEM image of slightly lithiated sample ($L_{1.05}$NMO). Regions at the edge part (Region I) and inner part (Region II) were selected and investigated. Mixed phases of LNMO and L_2NMO were verified at Region I according to the fast Fourier transform (FFT) image (Fig. 2b). Planes with distances of 0.15 and 0.21 nm with an angle of 45° were observed, which could be ascribed to (04-4) and (040) planes for LNMO phase. Besides, (022) and (013) planes for L_2NMO phase were also shown, as evidenced by the plane distances of 0.24 and 0.26 nm with an angle of 30° (Fig. 2b). The distribution of LNMO and L_2NMO phases was further investigated by inverse FFT image (Fig. 2c). Nanodomains with hybrid LNMO and L_2NMO phases in several nanometers were observed and cross-linked with each other at the edge part of the active material. In contrast, pure LNMO phase was shown at region II with (04–4) and (00–4) planes and no signals for L_2NMO phase were observed.

With higher overlithiation degree, only L_2NMO phase was observed at the edge part of $L_{1.4}$NMO particle (Fig. 2e-g, Fig. S6). A set of lattice fringes of 0.21 and 0.24 nm with an angle of 55° corresponded to (2–20) and (20–2) planes of L_2NMO phase (Fig. 2g), which was also observed in the FFT image of pure L_2NMO sample (Fig. 1h). In summary, L_2NMO phase existed at the edge region for L_{1+x}NMO sample with low overlithiation degree, which would spread over the entire edge region with increased overlithiation degree, and could further penetrate into the inner of the particle with higher overlithiation degree. At the optimal overlithiation degree, $L_{1.4}$NMO sample only showed LNMO phase after its initial charge to 4.5 V (Fig. S7). The complete conversion of L_2NMO phase to LNMO phase and the structural recovery indicated high reversibility of $L_{1.4}$NMO sample. The structural evolution of LNMO accompanied with overlithiation was schematically depicted in Fig. 2h according to the above analysis.

The elements and their chemical states were investigated by X-ray photoelectron spectroscopy (XPS). The signal intensity for Li element gradually increased with the increase of overlithiation degree (Fig. S8). High-resolution Li 1s spectra of $L_{1.4}$NMO sample with varying sputtering time were recorded. The sample before Ar^+ sputtering displayed the highest signal intensity for the peak at 54.4 eV, which gradually degraded with the increase of sputtering time from 0 to 20 min (Fig. 3a). The recorded Li content of $L_{1.4}$NMO sample gradually decreased from 45.0 at % to 30.0 at % and 22.4 at % and finally decreased to 14.2 at % with increasing sputtering time (0, 10, 20 and 60 min, Fig. 3b), which indicated that the $L_{1.4}$NMO sample possessed Li-rich surface structure. Fig. 3d compared the Li contents in LNMO, $L_{1.4}$NMO and L_2NMO samples after 10 and 60 min sputtering time. The Li content remained constant after different sputtering time for both LNMO and L_2NMO samples.

We also compared the high-resolution Mn 2p spectra for LNMO, $L_{1.4}$NMO and L_2NMO samples. The binding energy of Mn 2p provided information for different chemical states of Mn element. The Mn 2p peak for LNMO sample suggested the predominate ratio of Mn^{4+}. During the increase of overlithiation degree, the ratio of Mn^{4+} (643 and 654.5 eV) to Mn^{3+} (641.8 and 653.2 eV) was gradually decreased in L_{1+x}NMO samples, and dominated Mn^{3+} was shown in the high-resolution Mn 2p spectra for L_2NMO sample [28,29]. The formation of too much Mn^{3+} in structure would bring a negative effect on maintaining the structural stability, due to the Jahn–Teller distortion and disproportionation reaction during electrochemical cycling ($2\ Mn^{3+} \rightarrow Mn^{4+} + Mn^{2+}$) [30–33]. The chemical state of Ni element was shown in Fig. 3e, which displayed Ni $2p_{1/2}$ and $2p_{3/2}$ signals. The binding energy of Ni 2p ($2p_{3/2}$ at 854.7 eV and $2p_{1/2}$ at 871.9 eV) for $L_{1.4}$NMO sample was similar to that for LNMO ($2p_{3/2}$ at 855.0 eV and $2p_{1/2}$ at 872.2 eV), suggesting negligible effect of the chemical lithiation process on the chemical state of Ni element. The above analysis also verified the Li-rich interphase of partially overlithiated L_{1+x}NMO sample and the gradual overlithiation process from surface to inner, well in agreement with the TEM investigation.

To investigate the effect of overlithiation-induced structural evolution on the electrochemical behavior, L_{1+x}NMO samples with different overlithiation degrees were subject to electrochemical charge/discharge measurement. The capacity of L_{1+x}NMO samples during the first charge process gradually increased with the increase of overlithiation degree (Fig. 4a). When the overlithiation degree (x) was less than 0.4, the pre-inserted additional capacity mainly deintercalated at ~2.9 V (*vs.* Li/Li^+, ~29 mAh g^{-1} for $L_{1.2}$NMO and ~42 mAh g^{-1} for $L_{1.4}$NMO) during the first charge process. While the overlithiation degree (x) reached higher

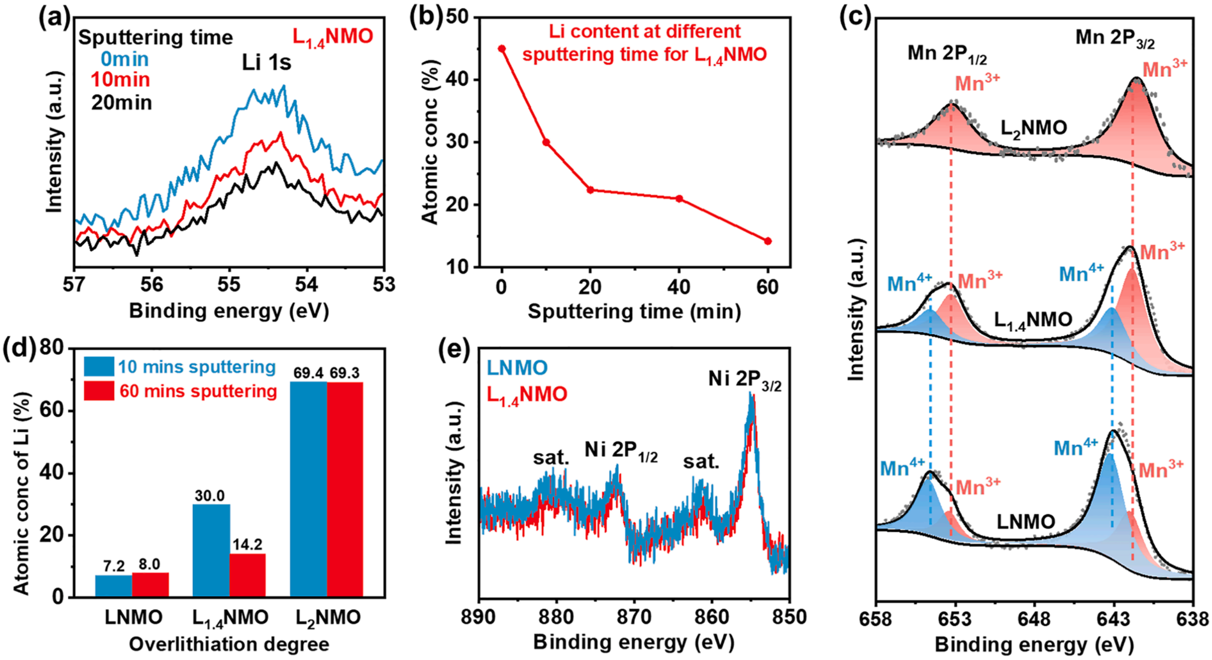

Fig. 3. (a) High-resolution Li 1 s spectra of $L_{1.4}$NMO sample. (b) The Li content in $L_{1.4}$NMO sample via XPS analysis. (c) High-resolution Mn 2p spectra of LNMO, $L_{1.4}$NMO and L_2NMO samples. (d) Element atomic concentration of Li for LNMO, $L_{1.4}$NMO and L_2NMO samples via XPS analysis. (e) High-resolution Ni 2p spectra of LNMO and $L_{1.4}$NMO samples.

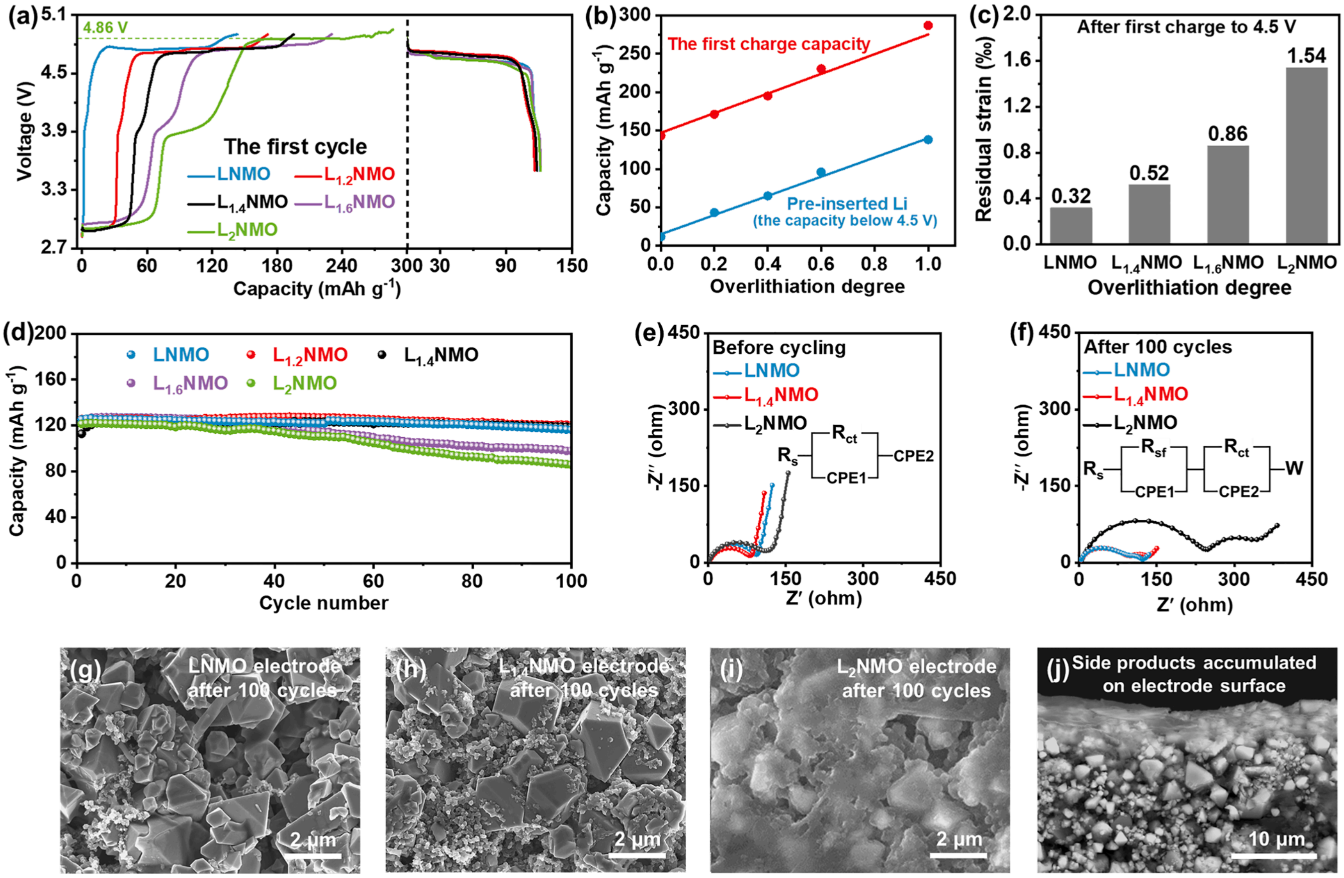

Fig. 4. (a) Voltage-capacity profiles of $L_{1+x}NMO$ ($x = 0$, 0.2, 0.4, 0.6 and 1) electrodes for the first cycle at 0.1 *C*. (b) Capacities of $L_{1+x}NMO$ electrodes during the first charge process. (c) Residual strain of $L_{1+x}NMO$ after the initial charge to 4.5 V according to the XRD refined results. (d) Cycling performance of $L_{1+x}NMO$ ($x = 0$, 0.2, 0.4, 0.6 and 1) electrodes at 0.5 *C*. EIS spectra of LNMO, $L_{1.4}NMO$ and L_2NMO electrodes (e) before cycling and (f) after 100 cycles (the inset was the corresponding equivalent circuit). (g)–(i) Top-view SEM images of (g) LNMO, (h) $L_{1.4}NMO$, (i) L_2NMO electrodes after 100 cycles. (j) Cross-sectional SEM image of L_2NMO electrode after 100 cycles.

than 0.6, the increased charge capacity was mainly contributed by the voltage slope at ~4.0 V (~18 mAh g^{-1} for $L_{1.6}NMO$ *vs.* ~43 mAh g^{-1} for L_2NMO). These newly formed voltage plateaus/slopes at ~2.9 and ~4.0 V correspond to the oxidation of Mn^{3+} to Mn^{4+}, due to the pre-insertion of additional Li ions [34]. Nearly all the pre-inserted Li in the measured $L_{1+x}NMO$ samples was extracted below 4.5 V (*vs.* Li/Li^+) in the first charge process and similar discharge capacities were observed for all the $L_{1+x}NMO$ samples with different overlithiation degrees (Fig. 4a, b and Table S2). These results suggest that once the overlithiation-induced extra Li was extracted during the initial charge process, it did not take part in the electrochemical cycling in the regular working voltage window of LNMO, and overlithiation would not sacrifice the reversible capacity of LNMO. It is worth noting that L_2NMO sample with the highest overlithiation degree endured a slightly higher charge plateau up to 4.86 V than that of other samples (Fig. 4a). Such result was also confirmed by differential capacity versus voltage (dQ/dV) profiles (Fig. S9). Compared to the peak value of 4.76 V for LNMO and $L_{1.4}NMO$ electrodes, the peak for L_2NMO electrode showed a shift to a higher potential of 4.87 V (*vs.* Li/Li^+) in the dQ/dV profiles, and it recovered to normal value in the following cycles (Fig. S10). The introduction of more extra Li beyond the tolerance of structure intensifies lattice strain of L_2NMO, and induces the formation of numerous grain boundaries and defaults, which could lead to higher overpotential for initial Li extraction. On the other hand, the residual Li species on sample surface after chemical overlithiation would react with ambient moisture and CO_2 to produce Li_2CO_3 when exposed to ambient air for electrode fabrication (Fig. S11), which could increase the overpotential for Li extraction [43–45]. The L_2NMO sample possessed the highest lithiation degree and more residual Li species could be introduced to produce Li_2CO_3 during the electrode fabrication. The values of residual strain for LNMO, $L_{1.4}NMO$ and L_2NMO samples were shown in Fig. 4c according to the XRD Rietveld refinement results after their first charge to 4.5 V (Fig. S12). Residual strain value of 1.54 ‰ was observed for L_2NMO, much larger than 0.32 ‰ for LNMO, 0.52 ‰ for $L_{1.4}NMO$ and 0.86 ‰ for $L_{1.6}NMO$, respectively (Table S5). Moreover, L_2NMO sample displayed a lower intensity in XRD peaks for LNMO phase after the first charge to 4.5 V, in comparison to that of LNMO and $L_{1.4}NMO$ under the same test conditions (Fig. S12a), indicating reduced crystallinity of L_2NMO after the release of the pre-inserted Li [35,36]. The low lattice strain of $L_{1.4}NMO$ after Li release suggested its more robust structure, which could support stable electrochemical cycling.

The dependence of cycling stability on overlithiation degrees (x) of $L_{1+x}NMO$ samples was further conducted. The capacity-cycle number plots of $L_{1+x}NMO$ ($x = 0$, 0.2, 0.4, 0.6 and 1) electrodes were displayed in Fig. 4d. LNMO and $L_{1.2}NMO$ electrodes showed close initial discharge capacities of 125.5 ± 0.2 mAh g^{-1} at 0.5 *C* (1 *C* = 140 mA g^{-1}), and capacity retention of 94 ± 1.5 % for 100 cycles. $L_{1.4}NMO$ electrode presented reversible discharge capacity of 124.7 mAh g^{-1} after initial activation cycles, and highly reversible capacity of 118.6 mAh g^{-1} on the 100th cycle, with high capacity retention of 95.1 %. Typically, LNMO, $L_{1.2}NMO$ and $L_{1.4}NMO$ electrodes displayed highly overlapped curves for the 100th cycle (Fig. S13a), revealing similar electrochemical cycling stability for these $L_{1+x}NMO$ samples ($x = 0$, 0.2 and 0.4). When the overlithiation degree (x) was further increased to 0.6, $L_{1.6}NMO$

electrode displayed gradual capacity fading from 123.2 to 98 mAh g^{-1} after 100 cycles (Fig. 4d) with a much lower capacity retention of 79.5 %. Even more prominent performance decay was observed for L_2NMO electrode, which delivered the lowest capacity of 85.7 mAh g^{-1} after 100 cycles (Fig. 4d). Besides, a severe increase in overpotential was observed for L_2NMO electrode in comparison to that of LNMO, $L_{1.2}$NMO and $L_{1.4}$NMO electrodes according to the corresponding dQ/dV profiles of LNMO, $L_{1.4}$NMO and L_2NMO electrodes at the 100th cycle (Fig. S13b). The obvious negative effect of exceeding the overlithiation degree ($x = 0.6$ or higher) on electrochemical cyclability may be caused by the accumulation of structural strain, grain boundaries and Mn^{3+} species beyond the tolerance of materials structure. In our investigation, $L_{1.4}$NMO electrode delivered balanced capacity and electrochemical cycling stability, suggesting an optimal overlithiation degree. Thus, the LNMO, $L_{1.4}$NMO and L_2NMO samples were selected as the main objects to investigate the correlation between structural stability and overlithiation degree in our further investigation.

XRD investigation on LNMO, $L_{1.4}$NMO and L_2NMO electrodes after 100 cycles was carried out. The cycled L_2NMO electrode displayed relatively weaker diffraction peaks than the LNMO and $L_{1.4}$NMO electrodes (Fig. S14), suggesting that a reasonable overlithiation degree was critical for sustaining stable structure and deep overlithiation degree would inevitably induce structural degradation after over long cycles. Electrochemical impedance spectroscopy (EIS) was conducted to investigate the stability of the electrode-electrolyte interface. The quantitative analysis was carried out by fitting the Nyquist plots of LNMO, $L_{1.4}$NMO and L_2NMO electrodes with an equivalent circuit model (detailed results shown in Table S3 and S4). The three electrodes exhibited similar charge transfer resistance (R_{ct}) before cycling (Fig. 4e, Table S3). However, a larger surface film resistance (R_{sf}, associated with the ionic charge transfer at the electrode-electrolyte interface, 234.4 ohm) [37,38] and R_{ct} (85.1 ohm) was shown by L_2NMO electrode after 100 cycles, in comparison to that of LNMO and $L_{1.4}$NMO electrodes after 100 cycles (Fig. 4f and Table S4). This result verified severe degraded interface of the cycled L_2NMO electrode. The surface of the cycled electrodes was further elucidated by XPS, in which the cycled L_2NMO electrode displayed much weaker O-transition metals (TM) signal in comparison to $L_{1.4}$NMO electrode after 100 cycles [39], supporting thicker by-product layer on the surface of the cycled L_2NMO electrode (Fig. S15).

The morphological evolution of electrodes was characterized by SEM (Figs. 4g–j and S16). The LNMO and $L_{1.4}$NMO electrodes after 100 cycles exhibited a clean surface with intact particles of active materials (Fig. 4g and h), which were similar to the fresh counterparts before cycling (Fig. S17). In contrast, abundant by-products were formed and covered the surface of the cycled L_2NMO electrode (Fig. 4i and j), which should be ascribed to the detrimental side reactions between the active materials and electrolyte, responsible for the continuously increased impedance. The dissolution of transitional metals from the active materials after 100 cycles was also investigated by ICP-OES. The concentration of Mn and Ni elements in electrolyte for L_2NMO||Li cell (0.170 and 0.093 mg ml^{-1}, respectively) was over three times than that for LNMO||Li (0.035 and 0.008 mg ml^{-1}, respectively) and $L_{1.4}$NMO||Li cells (0.047 and 0.016 mg ml^{-1}, respectively) (Fig. S18). Also, the content of Mn element on the anode surface for L_2NMO cell was much higher than that of LNMO and $L_{1.4}$NMO cells based on the results of electron probe micro-analyzer (EPMA) measurement (Fig. S19) [40–42]. As a result, a conclusion can be drawn that the L_2NMO sample is not chemically stable and suffers from parasitic reactions with electrolyte, leading to degraded interface and violent dissolution of transitional metals.

According to the above analysis, the evolution of L_2NMO and $L_{1.4}$NMO on cycling is summarized in Fig. 5. The intercalation of extra Li beyond the tolerance of structure (especially for L_2NMO sample) intensifies lattice strain, induces numerous grain boundaries and immoderate reduction of Mn element. Thus, the instability of structure and side reactions between active materials and electrolyte would be significantly aggravated, resulting in the increase of interfacial impedance due to the fast dissolution of transition metals and the accumulation of detrimental side products on the electrode surface. The

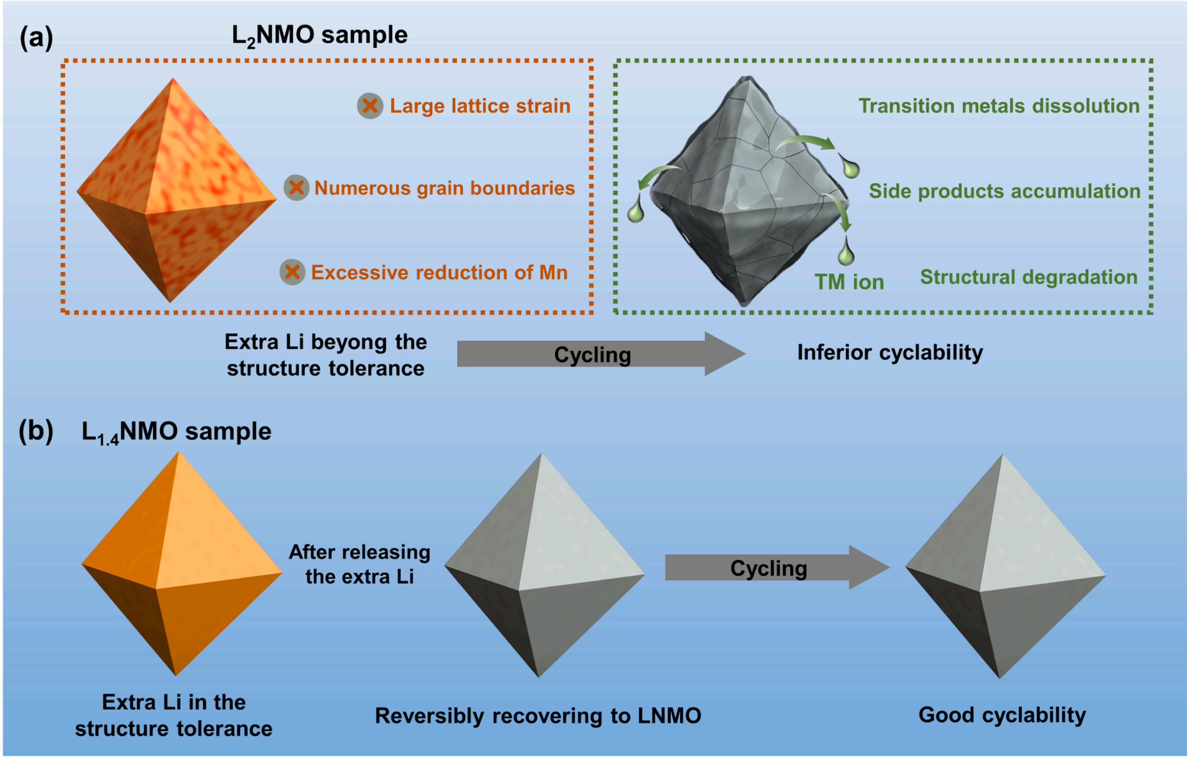

Fig. 5. The structural evolution of (a) L_2NMO and (b) $L_{1.4}$NMO electrodes after long-term cycling.

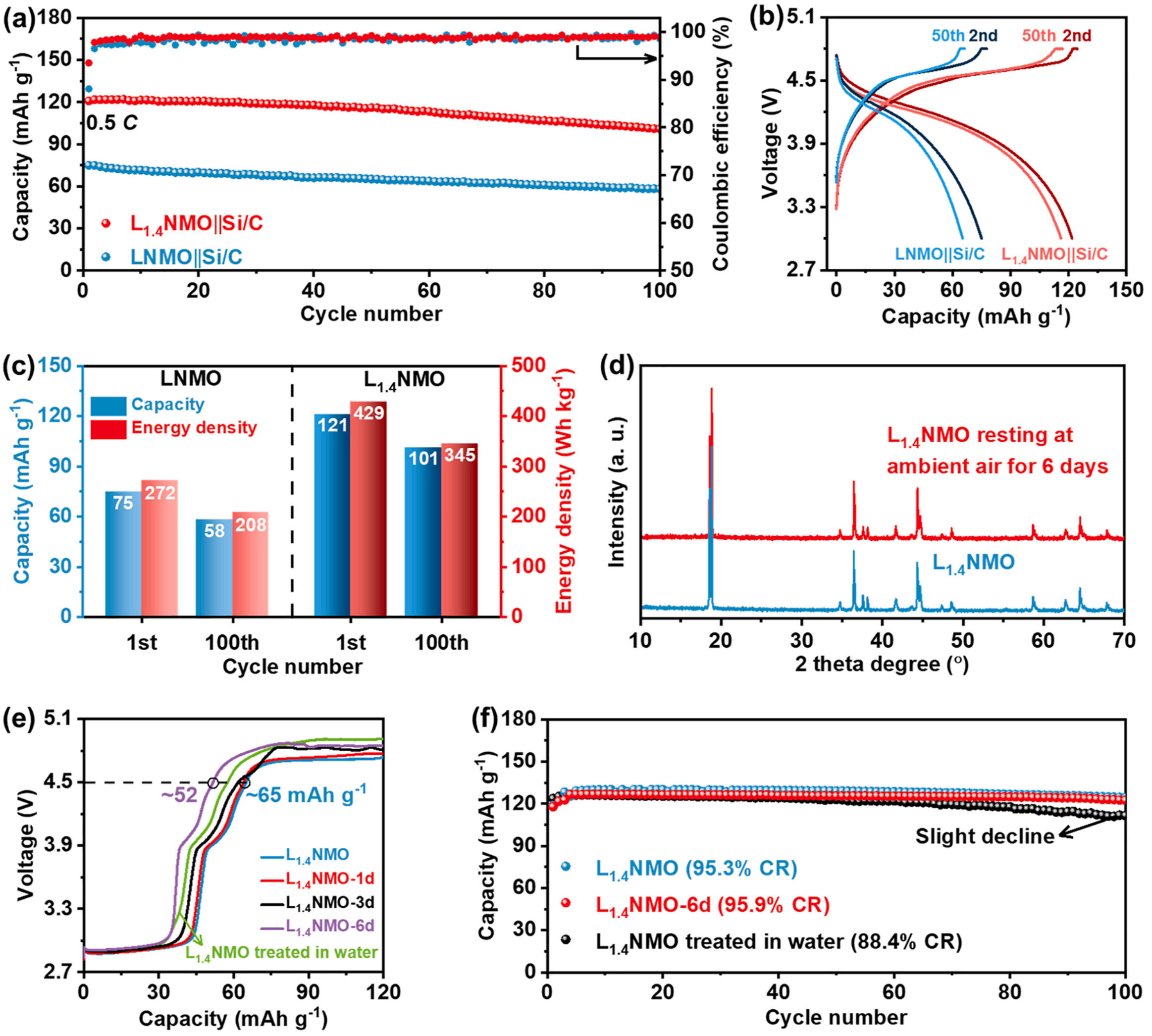

Fig. 6. (a) The capacity-cycle number and (b) voltage−capacity profiles of LNMO||Si/C and $L_{1.4}$NMO||Si/C cells at 0.5 *C*. (c) The discharge capacity and energy density of LNMO||Si/C and $L_{1.4}$NMO||Si/C cells before cycling and after 100 cycles. (d) XRD patterns of fresh $L_{1.4}$NMO and $L_{1.4}$NMO after resting at ambient air for 6 days. (e) The initial charge profile and (f) capacity-cycle number plots of $L_{1.4}$NMO electrode and $L_{1.4}$NMO electrodes after sensitivity test.

unbearable overlithiation degree finally leads to structural deterioration and rapid capacity fading (Fig. 5a). While for samples with rational overlithiation degree (such as $L_{1.4}$NMO), the side effect can be mitigated effectively, by virtue of good reversibility of crystal structure during the process of inserting and releasing the extra Li. With reasonable lattice strain and Mn^{3+}, $L_{1.4}$NMO offers comparable electrochemical cycling stability to the pristine LNMO (Fig. 5b).

The $L_{1.4}$NMO cathode was coupled with Si/C anode to fabricate full cells. Since the employed Si/C electrode possessed low ICE of ~75 % (Fig. S20a), full cell pairing cathode with extra active lithium could increase the overall capacity and energy density of batteries. As expected, the $L_{1.4}$NMO||Si/C cell presented a much higher reversible discharge capacity of 121.7 mAh g^{-1} than that of 74.9 mAh g^{-1} for the LNMO||Si/C cell at the second cycle at 0.5 *C* after activation (Fig. 6a), giving considerable 62.5 % capacity improvement. Moreover, the $L_{1.4}$NMO||Si/C cell displayed comparable cycling stability to LNMO||Si/C cell (capacity retention of 83.5 and 77.6 % for the 100 cycle, respectively). The good electrochemical stability of $L_{1.4}$NMO electrode was again verified by electrochemical measurement with full-cell configuration, in good agreement with the results of half cell measurement (Fig. 4a). The energy density of the full cells increased from 272 Wh kg^{-1} for the LNMO||Si/C cell to 429 Wh kg^{-1} for the $L_{1.4}$NMO||Si/C cell (calculated based on the total mass of cathode and anode active materials), delivering 57.8 % improvement (Fig. 6c). After 100 cycles, the $L_{1.4}$NMO||Si/C full cell displayed high energy density of 345 Wh kg^{-1}, which was still much higher than that of the initial energy density of LNMO||Si/C cell.

Typically, active materials with high lithium content are often moisture sensitive (e.g., Li_xSi and Li_xC), which could not endure long-time storage in ambient air, not to mention in direct contact with liquid water, which tremendously hinders practical implantation in industry manufacture. We investigated the tolerance of $L_{1.4}$NMO electrode against ambient air with ~60 % relative humidity (60 % RH), a harsher condition than that of industry manufacturing standard. After resting for 3 days, the $L_{1.4}$NMO electrode (denoted as $L_{1.4}$NMO-3d) delivered a similar capacity to the fresh counterpart below 4.5 V (this partial capacity was mostly contributed by pre-inserted Li) for the initial charge process (Fig. 6e). One thing needs to be mentioned is that $L_{1.4}$NMO electrode displays higher charging plateau after exposure to ambient air (Fig. 6e), which could be explained by the formation of Li_2CO_3 on its surface. It is common phenomenon that the Ni-rich layered oxides could react with atmospheric moisture and CO_2 to produce Li_2CO_3 [46–48], which induced the increase of overpotential during the initial charging process [43–45]. Li_2CO_3 could also be produced on the overlithiated LNMO surface due to the existence of relatively active Li-rich layer (L_2NMO layer). According to the results of Fourier transform infrared

(FT-IR) spectroscopy and XPS, the signals of Li_2CO_3 were detected for the $L_{1.4}$NMO sample after resting in ambient air for 3 days (Fig. S21a and b). Meanwhile, it was observed that the surface of $L_{1.4}$NMO-3d particle got coarse in comparison to the fresh counterpart (Figs. S17b and S21c) and the initial charging capacity of the $L_{1.4}$NMO was gradually decreased after prolonging the exposure time in ambient air (Fig. 6e). However, even after 6 days resting, the $L_{1.4}$NMO electrode could still retain 80 % additional capacity (~52 mAh g^{-1}, compared to the capacity of ~65 mAh g^{-1} for fresh $L_{1.4}$NMO) accompanied with similar electrochemical cyclability to fresh $L_{1.4}$NMO (Fig. 6e and f), which suggested that prepared $L_{1.4}$NMO sample possessed strong resistance to humid air. When treated in water for 10 s (washed with ethanol and dried in vacuum), the $L_{1.4}$NMO electrode only displayed a little capacity loss and slight decline with comparable capacity retention of 88.4% after 100 cycles (Fig. 6f). This again supported its good moisture resistance and chemical stability.

3. Conclusion

In summary, the overlithiation-dependent structure of LNMO cathode materials was investigated, including phase, lattice strain and grain boundary, as well as their effect on electrochemical properties. It was revealed that lattice strain and grain boundaries were produced accompanied by the overlithiation. Deep overlithiation of LNMO (e,g., L_2NMO) would therefore cause fast structural degradation and accelerated parasitic reaction with electrolyte, which further resulted in the dissolution of transition metals and rapid increase of interphase impendence, although high donable lithium ion capacity (e.g., additional 143.7 mAh g^{-1} for L_2NMO) was introduced. Experimentally, $L_{1.4}$NMO reached a balance between adequately donable lithium-ion capacity and cycling stability. Coupled with Si/C anode, $L_{1.4}$NMO||Si/C cell showed signficantly higher capacity than LNMO||Si/C cell (121.7 mAh g^{-1} *vs.* 74.9 mAh g^{-1}). The energy density of $L_{1.4}$NMO||Si/C cell increased to 429 Wh kg^{-1} from that of LNMO||Si/C cell (272 Wh kg^{-1}), amounting for 57.7 % improvement. Taking advantages of high voltage plateau and stable structure, $L_{1.4}$NMO exhibited good compatibility with low ICE anode and was thus promising to achieve high energy density. Furthermore, $L_{1.4}$NMO possessed extraordinary tolerance against ambient air. Even resting at 60 % RH air for 6 days, $L_{1.4}$NMO cell still retained the 80% amount of pre-inserted Li and achieved remarkable cyclability, indicating strong chemical stability.

4. Experimental section

4.1. Materials preparation

The chemical reductive solution of 0.5 M Naph-Li was prepared by dissolving naphthalene and metallic Li in tetrahydrofuran (THF) solvent with molar ratio of 1:1. Commercial LNMO powder was dispersed into the as-fabricated Naph-Li solution, followed by resting for 10 hours under contineous stirring at ~70 °C in a sealed container. After centrifugal separation, the L_{1+x}NMO product was washed with THF and dried in vacuum at 80 °C for 10 h. During the fabrication of L_{1+x}NMO electrode, 85 wt % active material, 7.5 wt % carbon black (CB) and 7.5 wt % polyvinylidene fluoride (PVDF) were mixed in N-methyl-2-pyrrolidone (NMP) solvent. The slurry was casted on aluminium foil and dried at 80°C for 10 h under vacuum. The Si/C electrode consisted of 80 wt % active material, 10 wt % CB, and 10 wt % Polyacrylic acid (PAA), which was fabricated using similar procedure to L_{1+x}NMO cathode.

$$LiNi_{0.5}Mn_{1.5}O_4 + x\ \text{Li-Naph} \rightarrow Li_{1+x}Ni_{0.5}Mn_{1.5}O_4 + x\ \text{Naph}$$

4.2. Electrochemical characterizations

Electrochemical evaluation of the L_{1+x}NMO electrodes was carried out using half cell and full cell configuration (CR2032 coin cells). The areal mass loading of cathode was ~9 mg cm^{-2}. Considering capacity decay on cycling for the employed Si/C electrode (Fig. S20b), a slightly high capacity ratio of negative to positive electrode (1.25) was adopted to ensure good cycling stability of full cells. The electrolyte was $LiPF_6$ in mixture of ethylene carbonate (EC) and diethyl carbonate (DEC) (1:1, by volume) with 5 % fluorinated ethylene carbonate (FEC). All the cells were activated at 0.1 *C* for first three cycles. The energy density was calculated based on total mass of cathode and anode of cells. The batteries cycling tests were conducted on a LAND 8-channel battery tester (CT-3001A) and Neware Battery Tester. The electrochemical impedance spectroscopy (EIS) measurements were carried on Biologic VMP3 electrochemical workstation.

4.3. Materials characterizations

X-ray diffraction (XRD) patterns were collected on a PANalytical B. V. instrument with Cu Kα1 radiation (λ = 1.5406 Å, 40 kV, 40 mA). The XRD data refinements were performed by using the FULLPROF suite software, based on the Rietveld method. Zeiss G300 scanning electron microscope (SEM) and transmission electron microscope (TEM, Tecnai G2 F30) were employed to investigate the morphology and structure of materials. X-ray photoelectron spectroscopy (XPS) measurements were performed on AXIS SUPRA+ with Al Kα radiation. Elemental analysis was conducted by Electron probe micro-analyzer (EPMA, EPMA-8050G). Fourier transform infrared (FT-IR) spectroscopy was performed on Nicolet iS10 FT-IR. The ICP-OES was conducted on 700 Series from Agilent Technologies.

CRediT authorship contribution statement

Yuchen Tan: Investigation, Data curation, Methodology, Writing – original draft, Writing – review & editing. **Rui Wang:** Data curation, Methodology, Writing – review & editing. **Xiaoxiao Liu:** Investigation, Methodology, Writing – review & editing. **Junmou Du:** Writing – original draft, Writing – review & editing. **Wenyu Wang:** Data curation, Writing – review & editing. **Renming Zhan:** Investigation, Writing – review & editing. **Shuibin Tu:** Investigation, Writing – review & editing. **Kai Cheng:** Data curation, Writing – review & editing. **Zihe Chen:** Data curation, Writing – review & editing. **Zhongyuan Huang:** Writing – review & editing, Writing – original draft. **Yinguo Xiao:** Methodology, Writing – review & editing. **Yongming Sun:** Supervision, Conceptualization, Data curation, Methodology, Writing – review & editing.

Declaration of Competing Interest

The authors declare no conflict of interest.

Data availability

No data was used for the research described in the article.

Acknowledgments

Y. Tan and R. Wang contribute equally to this work. This work was supported by the National Natural Science Foundation of China (Grant No. 52072137). The authors would like to thank the Analytical and Testing Center of Huazhong University of Science and Technology for providing the facilities to conduct the characterizations.

Supplementary materials

Supplementary material associated with this article can be found, in the online version, at doi:10.1016/j.ensm.2023.102962.

References

[1] A. Manthiram, K. Chemelewski, E.S. Lee, A perspective on the high-voltage $LiMn_{1.5}Ni_{0.5}O_4$ spinel cathode for lithium-ion batteries, Energy Environ. Sci. 7 (2014) 1339.

[2] N.M. Jobst, N. Paul, P. Beran, M. Mancini, R. Gilles, M. Wohlfahrt-Mehrens, P. Axmann, Dynamic structure evolution of extensively delithiated high voltage spinel $Li_{1+x}Ni_{0.5}Mn_{1.5}O_4$ $x< 1.5$, J. Am. Chem. Soc. 145 (2023) 4450.

[3] G.M. Liang, E. Olsson, J.S. Zou, Z.B. Wu, J.X. Li, C.Z. Lu, A.M. D`Angelo, B. Johannessen, L. Thomsen, B. Cowie, V.K. Peterson, Q. Cai, W.K. Pang, Z.P. Guo, Introducing 4*s*–2*p* orbital hybridization to stabilize spinel oxide cathodes for lithium-ion batteries, Angew. Chem. Int. Ed. 134 (2022), e202201969.

[4] H.J. Lee, X.X. Liu, Y. Chart, P. Tang, J.G. Bae, S. Narayanan, J.H. Lee, R.J. Potter, Y. M. Sun, M. Pasta, $LiNi_{0.5}Mn_{1.5}O_4$ cathode microstructure for all-solid-state batteries, Nano Lett. 22 (2022) 7477.

[5] W.L. Yao, M. Chouchane, W.K. Li, S. Bai, Z. Liu, L.T. Li, A.X. Chen, B. Sayahpour, R. Shimizu, G. Raghavendran, M.A. Schroeder, Y.T. Chen, D.H.S. Tan, B. Sreenarayanan, C.K. Waters, A. Sichler, B. Gould, D.J. Kountz, D.J. Lipomi, M. H. Zhang, Y.S. Meng, A 5V-class cobalt-free battery cathode with high loading enabled by dry coating, Energy Environ. Sci. (2023).

[6] H.T. Shen, Y.L. An, Q.Y. Man, J.Y. Wang, C.K. Liu, B.J. Xi, S.L. Xiong, J.K. Feng, Y. T. Qian, Controlled prelithiation of siloxene nanosheet anodes enables high performance 5 V-class lithium-ion batteries, Chem. Eng. J. 454 (2023), 140136.

[7] Z.H. Cui, F. Zou, H. Celio, A. Manthiram, Paving pathways toward long-life graphite/$LiNi_{0.5}Mn_{1.5}O_4$ full cells: electrochemical and interphasial points of view, Adv. Funct. Mater. 32 (2022), 2203779.

[8] Y.F. Shen, J.M. Zhang, Y.F. Pu, H. Wang, B. Wang, J.F. Qian, Y.L. Cao, F.P. Zhong, X.P. Ai, H.X. Yang, Effective chemical prelithiation strategy for building a silicon/sulfur Li-ion battery, ACS Energy Lett. 4 (2019) 1717.

[9] Y.S. Su, J.K. Chang, Polycyclic aromatic hydrocarbon-enabled wet chemical prelithiation and presodiation for batteries, Batteries 8 (2022) 99.

[10] I.W. Seong, K.T. Kim, W.Y. Yoon, Electrochemical behavior of a lithium-pre-doped carbon-coated silicon monoxide anode cell, J. Power Sources 189 (2009) 511.

[11] N. Liu, L.B. Hu, M.T. McDowell, A. Jackson, Y. Cui, Prelithiated silicon nanowires as an anode for lithium ion batteries, ACS Nano 5 (2011) 6487.

[12] H.J. Kim, S. Choi, S.J. Lee, M.W. Seo, J.G. Lee, E. Deniz, Y.J. Lee, E.K. Kim, J. W. Choi, Controlled prelithiation of silicon monoxide for high performance lithium-ion rechargeable full cells, Nano Lett. 16 (2016) 282.

[13] F. Wang, B. Wang, Z.L. Yu, C.Y. Zhu, P. Liu, J.X. Li, B. Wang, Y. Zhou, D.L. Wang, H.K. Liu, S.X. Dou, Construction of air-stable pre-lithiated SiO_x anodes for next-generation high-energy-density lithium-ion batteries, Cell Rep. Phys. Sci. 3 (2022), 100872.

[14] J. Jang, I. Kang, J. Choi, H. Jeong, K.W. Yi, J. Hong, M. Lee, Molecularly tailored lithium–arene complex enables chemical prelithiation of high-capacity lithium-ion battery anodes, Angew. Chem. Int. Ed. 59 (2020) 14473.

[15] G.W. Wang, F.F. Li, D. Liu, D. Zheng, Y. Luo, D.Y. Qu, T.Y. Ding, D.Y. Qu, Chemical prelithiation of negative electrodes in ambient air for advanced lithium-ion batteries, ACS Appl. Mater. Interfaces 11 (2019) 8699.

[16] K. Takei, K. Kumai, Y. Kobayashi, H. Miyashiro, T. Iwahori, T. Uwai, H. Ue, An X-ray photoelectron spectroscopy study on the surface film on carbon black anode in lithium secondary cells, J. Power Sources 54 (1995) 171.

[17] L.D. Lin, K. Qin, Q.H. Zhang, L. Gu, L.M. Suo, Y.S. Hu, H. Li, X.J. Huang, L.Q. Chen, Li-rich $Li_2[Ni_{0.8}Co_{0.1}Mn_{0.1}]O_2$ for anode-free lithium metal batteries, Angew. Chem. Int. Ed. 60 (2021) 8289.

[18] X.X. Liu, Y.C. Tan, W.Y. Wang, C.H. Li, Z.W. Seh, L. Wang, Y.M. Sun, Conformal prelithiation nanoshell on $LiCoO_2$ enabling high-energy lithium-ion batteries, Nano Lett. 20 (2020) 4558.

[19] Z.Z. Liu, S.B. Ma, X. Mu, R.L. Li, G.P. Yin, P.J. Zuo, A scalable cathode chemical prelithiation strategy for advanced silicon-based lithium ion full batteries, ACS Appl. Mater. Interfaces 13 (2021) 11985.

[20] X.Y. Meng, Y.Z. Liu, L. Yu, J.S. Qiu, Z.Y. Wang, Air-stable Li_2S cathode for quasi-solid-state anode-free batteries with high volumetric energy, Adv. Funct. Mater. 33 (2022), 2211062.

[21] R.M. Zhan, X.C. Wang, Z.H. Chen, Z.W. Seh, L. Wang, Y.M. Sun, Promises and challenges of the practical implementation of prelithiation in lithium-ion batteries, Adv. Energy Mater. 11 (2021), 2101565.

[22] Z.W. Zhang, J.L. Yang, W. Huang, H.S. Wang, W.J. Zhou, Y.B. Li, Y.Z. Li, J.W. Xu, W.X. Huang, W. Chiu, Y. Cui, Cathode-electrolyte interphase in lithium batteries revealed by cryogenic electron microscopy, Matter 4 (2021) 302.

[23] L.D. Lin, K. Qin, M.Y. Li, Y.S. Hu, H. Li, X.J. Huang, L.Q. Chen, L.M. Suo, Spinel-related $Li_2Ni_{0.5}Mn_{1.5}O_4$ cathode for 5-V anode-free lithium metal batteries, Energy Storage Mater. 45 (2022) 821.

[24] K. Amine, H. Tukamoto, H. Yasuda, Y. Fujita, A new three-volt spinel $Li_{1+x}Mn_{1.5}Ni_{0.5}O_4$ for secondary lithium batteries, J. Electrochem. Soc. 143 (1996) 1607.

[25] M. Mancini, G. Gabrielli, P. Axmann, M. Wohlfahrt-Mehrens, Electrochemical performance and phase transitions between 1.5 and 4.9 V of highly-ordered $LiNi_{0.5}Mn_{1.5}O_4$ with tailored morphology: influence of the lithiation method, J. Electrochem. Soc. 164 (2016) A6229.

[26] G.K. Williamson, W.H. Hall, X-ray line broadening from filed aluminium and wolfram, Acta Metall. 1 (1953) 22.

[27] E.S. Lee, K.W. Nam, E.Y. Hu, A. Manthiram, Influence of cation ordering and lattice distortion on the charge–discharge behavior of $LiMn_{1.5}Ni_{0.5}O_4$ spinel between 5.0 and 2.0 V, Chem. Mater. 24 (2012) 3610.

[28] Y. Han, Y.S. Jiang, Y. Xia, L. Deng, L.F. Que, F.D. Yu, Z.B. Wang, Suppressed phase separation in spinel $LiNi_{0.5}Mn_{1.5}O_4$ cathode via interstitial sites modulation, Nano Energy 91 (2022), 106636.

[29] X. Ji, X.Y. Dai, F.Z. Wu, H.X. Jin, Liquid-phase integrated surface modification to construct stable interfaces and superior performance of high-voltage $LiNi_{0.5}Mn_{1.5}O_4$ cathode materials, ACS Sustain. Chem. Eng. 10 (2022) 9850.

[30] D.S. Lu, M.Q. Xu, L. Zhou, A. Garsuch, B.L. Lucht, Failure mechanism of graphite/$LiNi_{0.5}Mn_{1.5}O_4$ cells at high voltage and elevated temperature, J. Electrochem. Soc. 160 (2013) A3138.

[31] B. Michalak, B. Berkes, H. Sommer, T. Brezesinski, J.R. Janek, Electrochemical cross-talk leading to gas evolution and capacity fade in $LiNi_{0.5}Mn_{1.5}O_4$/graphite full-cells, J. Phys. Chem. C 121 (2017) 211.

[32] C. Jayawardana, N. Rodrigo, B. Parimalam, B.L. Lucht, Role of electrolyte oxidation and difluorophosphoric acid generation in crossover and capacity fade in lithium ion batteries, ACS Energy Lett. 6 (2021) 3788.

[33] M.X. Lin, L.B. Ben, Y. Sun, H. Wang, Z.Z. Yang, L. Gu, X.Q. Yu, X.Q. Yang, H. F. Zhao, R.C. Yu, M. Armand, X.J. Huang, Insight into the atomic structure of high-voltage spinel $LiNi_{0.5}Mn_{1.5}O_4$ cathode material in the first cycle, Chem. Mater. 27 (2015) 292.

[34] Z. Moorhead-Rosenberg, E. Allcorn, A. Manthiram, *In situ* mitigation of first-cycle anode irreversibility in a new spinel/FeSb lithium-ion cell enabled via a microwave-assisted chemical lithiation process, Chem. Mater. 26 (2014) 5905.

[35] Y.Z. Lv, Y.Z. Jin, Y. Xue, J. Wu, X.G. Zhang, Z.B. Wang, Electrochemical properties of high-voltage $LiNi_{0.5}Mn_{1.5}O_4$ synthesized by a solid-state method, RSC Adv. 4 (2014) 26022.

[36] N. Mokhtar, N.H. Idris, Comparison on electrochemical performances of $LiNi_{0.5}Mn_{1.5}O_4$ cathode materials synthesized using different precursors, Mater. Today Proc. 3 (2016) S129.

[37] Y. Wang, Q.H. Zhang, Z.C. Xue, L.F. Yang, J.Y. Wang, F.Q. Meng, Q.H. Li, H.Y. Pan, J.-N. Zhang, Z. Jiang, W.L. Yang, X.Q. Yu, L. Gu, H. Li, An *in situ* formed surface coating layer enabling $LiCoO_2$ with stable 4.6 V high-voltage cycle performances, Adv. Energy Mater. 10 (2020), 2001413.

[38] R. Gu, Z.T. Ma, T. Cheng, Y.C. Lyu, A. Nie, B.K. Guo, Improved electrochemical performances of $LiCoO_2$ at elevated voltage and temperature with an *in situ* formed spinel coating layer, ACS Appl. Mater. Interfaces 10 (2018) 31271.

[39] H.J. Lee, Z. Brown, Y. Zhao, J. Fawdon, W.X. Song, J.H. Lee, M. Pasta, Ordered $LiNi_{0.5}Mn_{1.5}O_4$ cathode in Bis(fluorosulfonyl)imide-based ionic liquid electrolyte: importance of the cathode–electrolyte interphase, Chem. Mater. 33 (2020) 1238.

[40] I.A. Shkrob, A.J. Kropf, T.W. Marin, Y. Li, O.G. Poluektov, J. Niklas, D.P. Abraham, Manganese in graphite anode and capacity fade in Li ion batteries, J. Phys. Chem. C 118 (2014) 24335.

[41] S.R. Gowda, K.G. Gallagher, J.R. Croy, M. Bettge, M.M. Thackeray, M. Balasubramanian, Oxidation state of cross-over manganese species on the graphite electrode of lithium-ion cells, Phys. Chem. Chem. Phys. 16 (2014) 6898.

[42] G.M. Liang, V.K. Peterson, K.W. See, Z.P. Guo, W.K. Pang, Developing high-voltage spinel $LiNi_{0.5}Mn_{1.5}O_4$ cathodes for high-energy-density lithium-ion batteries: current achievements and future prospects, J. Mater. Chem. A 8 (2020) 15373.

[43] R. Jung, R. Morasch, P. Karayaylali, K. Phillips, F. Maglia, C. Stinner, Y. Shao-Horn, H.A. Gasteiger, Effect of ambient storage on the degradation of Ni-rich positive electrode materials (NMC811) for Li-ion batteries, J. Electrochem. Soc. 165 (2018) A132.

[44] C.J. Lv, Z.G. Li, X.N. Ren, K.X. Li, J.M. Ma, X.C. Duan, Revealing the degradation mechanism of Ni-rich cathode materials after ambient storage and related regeneration method, J. Mater. Chem. A 9 (2021) 3995.

[45] A. Grenier, H. Liu, K.M. Wiaderek, Z.W. Lebens-Higgins, O.J. Borkiewicz, L.F. J. Piper, P.J. Chupas, K.W. Chapman, Reaction heterogeneity in $LiNi_{0.8}Co_{0.15}Al_{0.05}O_2$ induced by surface layer, Chem. Mater. 29 (2017) 7345.

[46] L.F. Zou, Y. He, Z.Y. Liu, H.P. Jia, J. Zhu, J.M. Zheng, G.F. Wang, X.L. Li, J. Xiao, J. Liu, J.G. Zhang, G.Y. Chen, C.M. Wang, Unlocking the passivation nature of the cathode–air interfacial reactions in lithium ion batteries, Nat. Commun. 11 (2020) 3204.

[47] Y. You, H. Celio, J.Y. Li, A. Dolocan, A. Manthiram, Modified high-nickel cathodes with stable surface chemistry against ambient air for lithium-ion batteries, Angew. Chem. Int. Ed. 57 (2018) 6480.

[48] N.V. Faenza, L. Bruce, Z.W. Lebens-Higgins, I. Plitz, N. Pereira1, L.F.J. Piper, G. G. Amatucci, Growth of ambient induced surface impurity species on layered positive electrode materials and impact on electrochemical performance, J. Electrochem. Soc. 164 (2017) A3727.